Experimental study on identifying cracks of increasing size using ultrasonic excitation

Jungeun An, Raphael T Haftka, Nam H Kim, Fuh-Gwo Yuan, Byung Man Kwak, Hoon Sohn and Chul Min Yeum

Structural Health Monitoring 2012 11: 95 originally published online 6 July 2011
DOI: 10.1177/1475921711406581

Article

SHM Structural Health Monitoring

Structural Health Monitoring
11(1) 95–108

DOI: 10.1177/1475921711406581
shm.sagepub.com
SAGE

Experimental study on identifying cracks of increasing size using ultrasonic excitation

Jungeun An[1], Raphael T Haftka[1], Nam H Kim[1], Fuh-Gwo Yuan[2], Byung Man Kwak[3], Hoon Sohn[4] and Chul Min Yeum[4]

Abstract

In structural health monitoring, crack identification using scattered ultrasonic waves from a crack is one of the most active research areas. Crack size estimation is important for judging the severity of the damage. If measurements are frequently performed as the crack grows, then a better estimation of crack size may be possible by analyzing sensor signals for the same crack location with different sizes. The objective of this article is to explore the relationship between the sensor signal amplitude and crack size through experiments and simulation for estimating the size. Cracks are machined into an aluminum plate and measurements are carried out with ultrasound excitation using piezoelectric transducer arrays that alternate their role as actuators or sensors. Initially, a hole of 2.5 mm diameter is drilled in the plate, and it is gradually machined to a crack with a size up to 50 mm. Signal amplitude is measured from the sensor arrays. The migration technique is used to image the crack and to find the crack location. The maximum received signal amplitude is found to vary linearly with size from simulation and this agrees with measurements with crack size up to 30 mm. The deviation between the simulation and experiment increases as the crack grows.

Keywords

structural health monitoring, machined cracks, migration technique, crack identification, size estimation

Introduction

The current state-of-the-art manual inspection is accurate; even some of sub-millimeter size cracks can be detected.[1] However, manual inspection is time consuming, and some inaccessible 'hot' spots require the structural parts to be disassembled. Thus, much research has been focusing on structural health monitoring (SHM), an integrated technology of assessing structural damage, using mounted or embedded sensors.[2–11]

Unlike manual inspections, SHM can continually trace a crack as it grows. This provides not only an opportunity for better diagnosis, but also more accurate prognosis because crack growth provides information on the evolution of the crack size. This article describes SHM measurements of a crack for a series of crack sizes using linearly distributed piezoelectric sensor arrays. The objective of this article is to explore a relationship between the size of a through-the-thickness crack and the signal amplitude from guided waves in plate structures generated from piezoelectric actuators.

Many damage identification techniques have been developed using various types of inspection methods such as guided Lamb wave,[3–5] natural frequency,[6–8] eddy current,[9,10] and fiber optics.[11] Methods based on ultrasonic guided wave propagation have shown

[1]Department of Mechanical and Aerospace Engineering, University of Florida, Gainesville, FL 32611, USA.
[2]Department of Mechanical and Aerospace Engineering, North Carolina State University, Raleigh, NC, USA.
[3]Department of Mechanical Engineering, KAIST, Daejeon, Korea.
[4]Department of Civil and Environmental Engineering, KAIST, Daejeon, Korea.

Corresponding author:
Jungeun An, Department of Mechanical and Aerospace Engineering, University of Florida, Gainesville, FL 32611, USA
Email: jean@ufl.edu

Table 1. Mechanical properties of aluminum plate

Young's modulus, E (GPa)	Poisson's ratio, ν	Density, ρ (kg/m^3)
72	0.3	2.73×10^3

Table 2. Properties of piezoelectric disc (modified PZT-4)

Geometry (mm)	Diameter:10.0, thickness:0.4
Density ρ (kg/m^3)	7.9×10^3
Young's modulus E (GPa)	E_{11}: 86, E_{33}: 73
Piezoelectric coefficient d_{31} (m/V)	-140×10^{-12}
Piezoelectric coefficient d_{33} (m/V)	320×10^{-12}
Piezoelectric coefficient g_{31} (Vm/N)	-11×10^{-3}
Piezoelectric coefficient g_{33} (Vm/N)	25×10^{-3}
Dielectric constant K_3	1400

promises in identifying general parameters involved in many types of flaws.[3–5]

There have been several techniques to determine the defect size accurately using ultrasonic waves. Time of flight diffraction (TOFD) is a well-known approach of determining the defect size and location in beams by using embedded PZT sensors;[12] other approaches were also made for beam structures.[13–15] For two-dimensional plate-like structures, the effect of flaw size on the scattered signal amplitude has been investigated in some research.[3,16,17] However, research has focused more on the location of damage rather than accurate size quantification, because size estimation will be limited without precise location of the damage, and this is one of the limitations of automated SHM.[18–23] For the location, we applied the migration technique developed by Wang and Yuan,[24] which employs a linear array of sensors that essentially examines the scattered profile as a pulse-echo in two-dimensional space, thus having an advantage in terms of identifying a crack in a plate by imaging it. A solid foundation has been established for the application of the migration technique for nearly a decade by both simulation and experiment.[24–29] With the imaging result, we can simply extract the crack location, and compare the experiment with simulation. In particular, we seek to explore the relationship between scattered signal amplitude and the size of the crack.

The remainder of this article is organized as follows. Second section describes the test procedure and third section describes how we simulate wave propagation. Fourth section discusses obtaining approximate location by imaging the crack using the migration technique. The comparison between experimental and simulation results for signal amplitude variation according to different crack sizes can be found in fifth section. This section also discusses the effect of relative crack location using another set of sensors in the experiment. Sixth section presents concluding remarks.

Test panel and test procedures

An Aluminum 6061 panel ($600 \times 600 \times 3.2\,\text{mm}^3$) was tested for examining the ability to estimate the size of a through-the-thickness crack. Table 1 shows the mechanical properties of the panel. In order to detect a crack, we used two sets of linear sensor/actuator arrays, with each set containing nine lead zirconate titanate (PZT) discs (diameter, 10 mm; thickness, 0.4 mm; Table 2). Each PZT disc can be a sensor or an actuator. The equally-spaced sensor arrays are attached to the plate by epoxy bond as shown in Figure 1(c) with 62.5 mm spacing, and the total length of sensor array is 500 mm. The two sets of linear arrays are used to study the effect of crack location. Figure 1(c) also shows a vertical array of sensors, which is not used for this article. When a PZT disc is used as an actuator, all other PZT discs in the array are used as sensors. The sensors at both ends (numbered 0 and 8) are not used as actuators but only as sensors. Thus, only seven PZTs are used as actuators to emit the ultrasonic signal into the plate, and the Lamb wave generated from the actuator is recorded at the remaining sensors for both the pristine and damaged states for every crack increment. The excitation from the PZT is a five-peaked toneburst signal. Scattered wavefield from the damage is calculated by the difference between the pristine and damaged states. The crack was manufactured first by drilling a 4.5-mm diameter hole centered at (−90 mm, −110 mm) at the center of the plate. Afterwards, we gradually increased the size of the damage to form a shape close to a straight crack up to 50 mm in length by machining (Figure 2). The 15 crack sizes tested are listed in Table 3.

The NI PXI-1000B system was used for data collection with the LabView program. The sampling rate was set to 5 MHz, and the signal resolution was 16-bit. Since the resulting signal amplitude from the sensors was very small, the Piezo Linear Amplifier EPA 104 with 7 dB gain was used (Figure 3). To reduce the effect of noise, the excitation from the PZT is repeated ten times and the sensor readings are averaged. This repetition can reduce the effect of random noise. As a result, the standard deviation of noise during pre-trigger has been reduced by approximately a factor of three. The scattered wave-field from the crack was obtained by subtracting the pristine plate signal from the signal from the damaged plate (Figure 4). Then, the maximum peak-to-peak amplitude of the scattered signal was identified. In addition, the migration

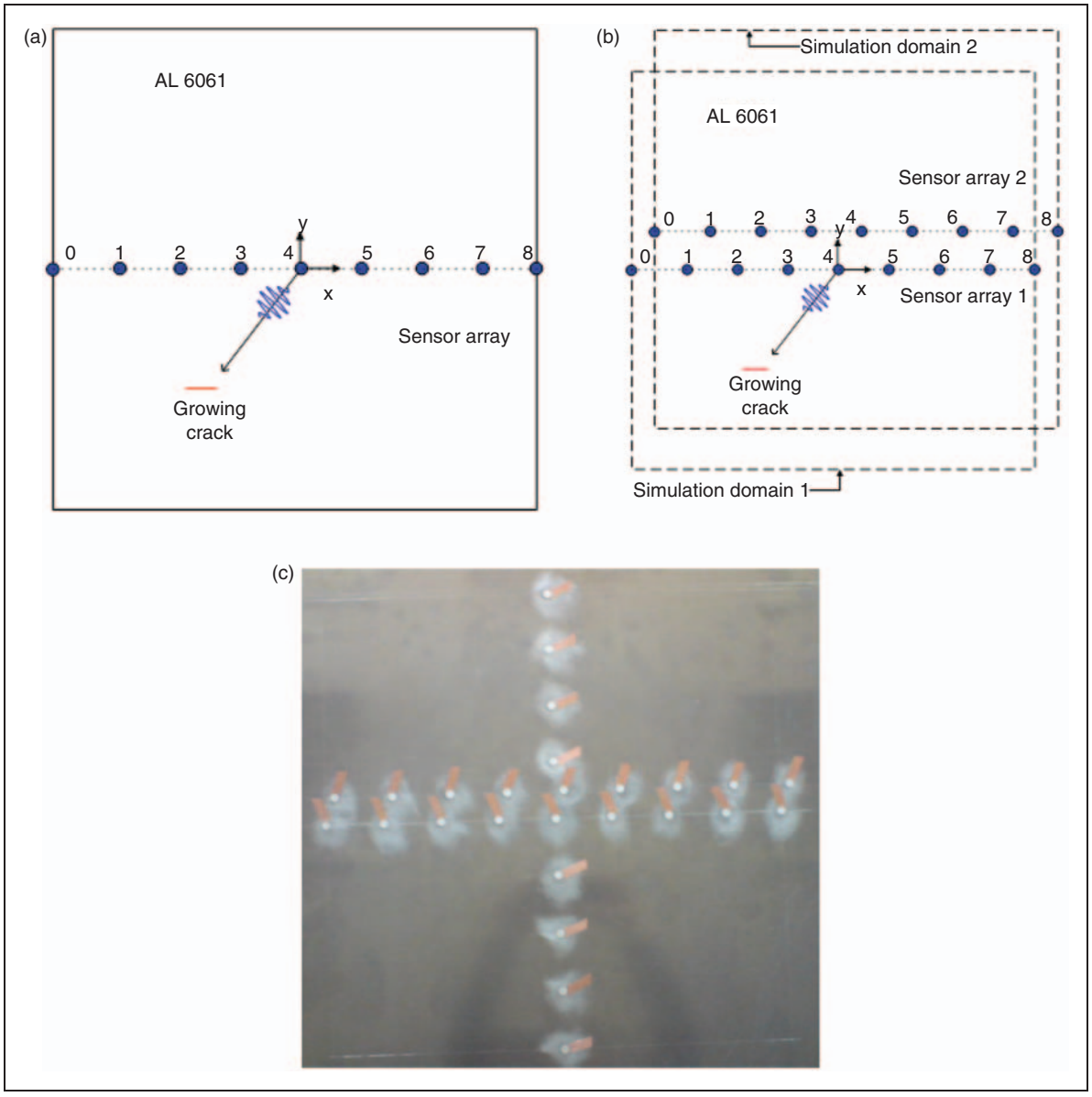

Figure 1. Layout of actuators and sensors: (a) one set of sensors for simulation and experiment; (b) two sensor arrays attached to the plate and their corresponding domain; and (c) aluminum 6061 test plate – pristine state. Three arrays of sensors are attached to the plate, but the vertical array is not employed in this research.

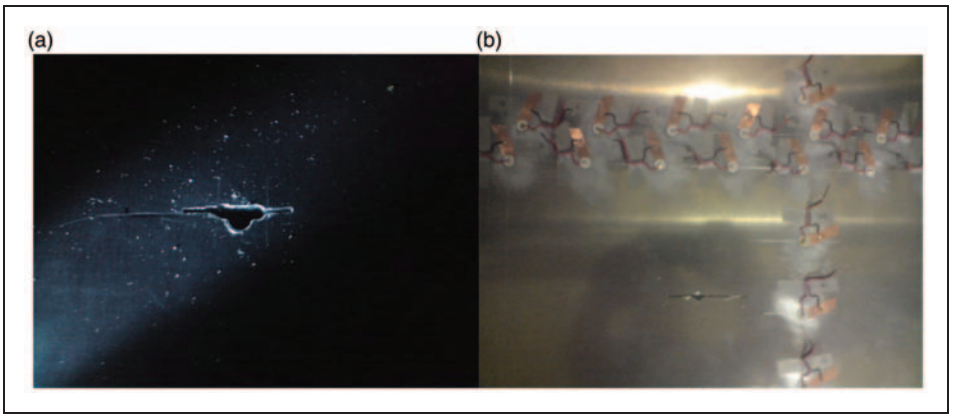

Figure 2. Damage manufactured to the plate: (a) 16 mm damage centered at (−90, −110) mm and (b) 50 mm machined crack.

technique was used to create an image of the damage for an approximate location of the crack. Migration technique compares the incident wavefield (direct signal) with the scattered wavefield (difference between responses from pristine and damaged plate) to identify the location of the crack. More details about the migration technique are given in the fourth section.

To determine the excitation frequency, a preliminary experiment was performed using an identical plate prior to actual testing. By using two piezoelectric transducers attached on the same location on the plate, but opposite sides through the thickness and a PZT sensor on the different location, we examined the amplitude difference due to different excitation frequencies. Because of the low value of the product of frequency and plate thickness, only the fundamental modes of symmetric and anti-symmetric waves, also known as S_0 and A_0 modes propagate in the plate. In this study, only the A_0 mode was used to examine the scattered signal since it has a larger amplitude than S_0 mode at the frequency of interest and is highly dispersive. The central frequency was chosen to be 110 kHz corresponding to the wavelength of 27 mm based on the result of this frequency–amplitude experiment, which gives the maximum amplitude of A_0 mode excitation (Figure 5(a)). The five-peaked toneburst used for wave excitation is shown in Figure 5(b).

Table 3. List of crack sizes (mm) tested

2.5 (hole)	13.8	31.5
3.0 (hole)	16.0	35.0
4.5 (hole)	18.0	40.0
9.0	21.0	45.0
11.0	26.0	50.0

Wavefield simulation

Governing equations of flexural waves

The governing equations of flexural waves are formulated, in this subsection, as a first-order system that models the waves using a finite difference scheme, described in the next subsection. Using the stress resultants (Q_x, Q_y, M_x, M_y, and M_{xy}) and the plate displacement components (w, ψ_x, and ψ_y), the equations of motion can be written as:

$$\begin{aligned} \frac{\partial Q_x}{\partial x} + \frac{\partial Q_y}{\partial y} + q &= \rho h \frac{\partial^2 w}{\partial t^2} \\ \frac{\partial M_x}{\partial x} + \frac{\partial M_{xy}}{\partial y} - Q_x &= \frac{\rho h^3}{12} \frac{\partial^2 \psi_x}{\partial t^2} \\ \frac{\partial M_{xy}}{\partial x} + \frac{\partial M_y}{\partial y} - Q_y &= \frac{\rho h^3}{12} \frac{\partial^2 \psi_y}{\partial t^2} \end{aligned} \tag{1a}$$

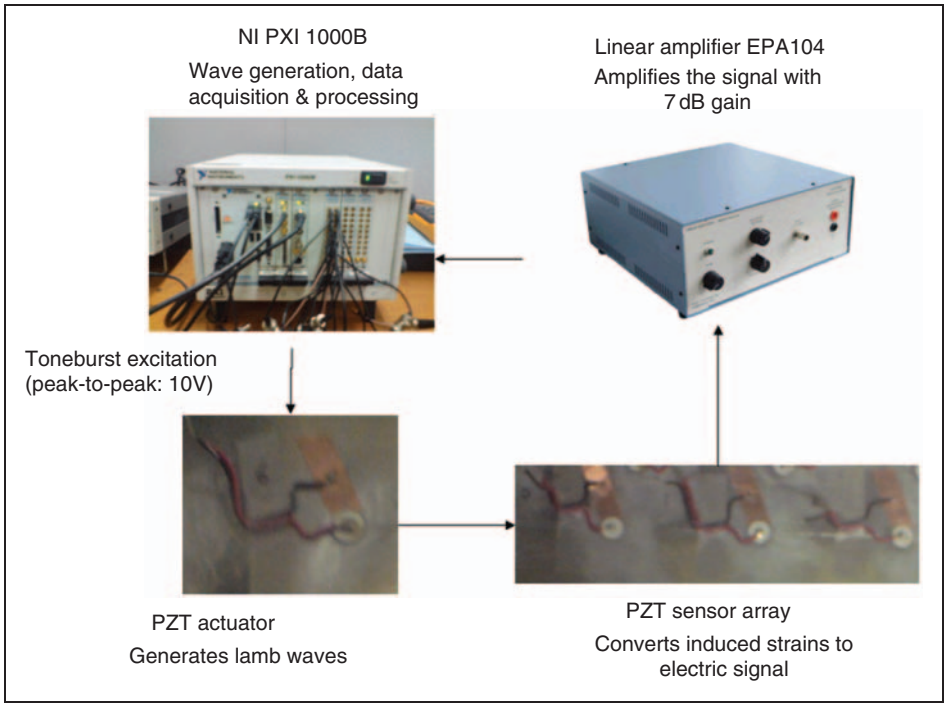

Figure 3. Signal generation and acquisition in the experimental set-up.

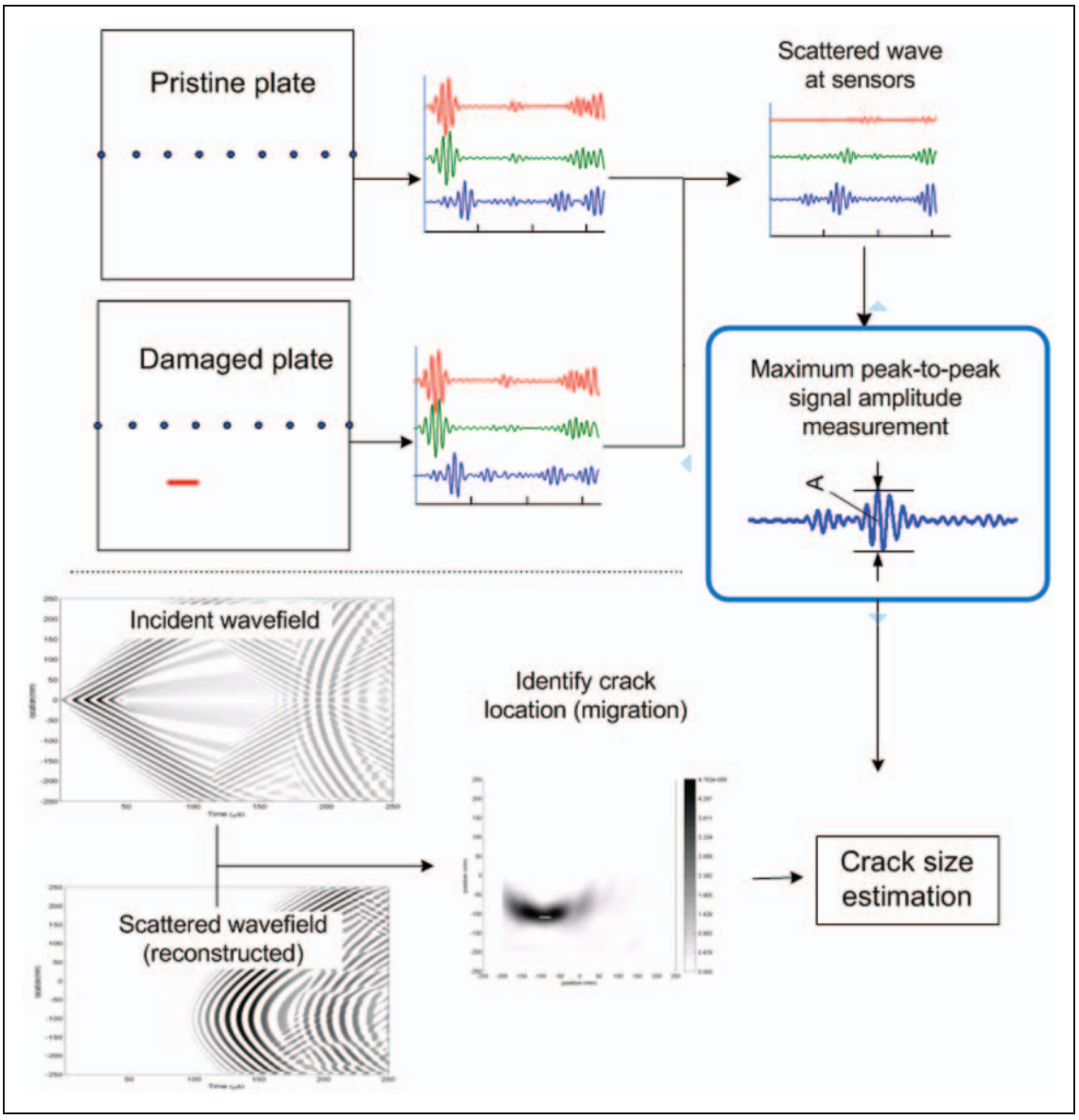

Figure 4. Test procedure for estimated location by migration technique and signal amplitude measurement.

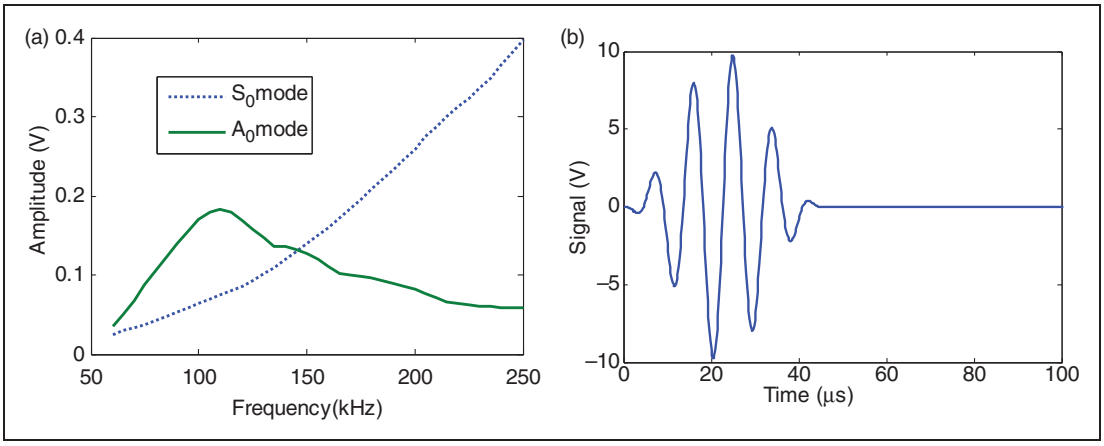

Figure 5. (a) Frequency sweep experiment. Amplitudes of transmitted signal are shown for A_0 mode and S_0 mode. (b) Five-peaked toneburst excitation sent to the actuator (110 kHz).

and the constitutive equations:

$$\begin{Bmatrix} M_x \\ M_y \\ M_{xy} \end{Bmatrix} = D \begin{bmatrix} 1 & \nu & 0 \\ \nu & 1 & 0 \\ 0 & 0 & \frac{1-\nu}{2} \end{bmatrix} \begin{Bmatrix} \frac{\partial \psi_x}{\partial x} \\ \frac{\partial \psi_y}{\partial y} \\ \frac{\partial \psi_x}{\partial y} + \frac{\partial \psi_y}{\partial x} \end{Bmatrix}$$

$$Q_x = \kappa^2 Gh\left(\frac{\partial w}{\partial x} + \psi_x\right)$$

$$Q_y = \kappa^2 Gh\left(\frac{\partial w}{\partial y} + \psi_y\right) \tag{1b}$$

In Equation (1), E and G are Young's modulus and shear modulus respectively, q is the transverse loading applied to the plate, h is the plate thickness, ν is the Poisson's ratio, ρ is the mass density, κ is a shear correction factor, $\kappa^2 = \pi^2/12$, and $D = Eh^3/[12(1-\nu^2)]$ is the flexural rigidity. Substituting the plate stress resultants in Equation (1b) into Equation (1a), the equations of motions in terms of plate displacement components can be obtained. Then, by eliminating ψ_x and ψ_y from the three motion equations, a single differential equation in terms of transverse displacement w can be written as:

$$\left(\nabla^2 - \frac{\rho}{G'}\frac{\partial^2}{\partial t^2}\right)\left(D\nabla^2 - \frac{\rho h^3}{12}\frac{\partial^2}{\partial t^2}\right)w + \rho h\frac{\partial^2 w}{\partial t^2} = \left(1 - \frac{D\nabla^2}{G'h} - \frac{\rho h^2}{12G'}\frac{\partial^2}{\partial t^2}\right)q(x,y,t) \tag{2}$$

where $G' = \kappa^2 G$. When the wave number is small and the thickness of the plate is substantially smaller than the wavelength, Equation (2) can be approximated by

$$D\nabla^4 w + \rho h\frac{\partial^2 w}{\partial t^2} = q(x,y,t) \tag{3}$$

Defining $\boldsymbol{u}^T = \{\dot{w}, \psi_x, \psi_y, Q_y, Q_x, M_x, M_y, M_{xy}\}$, $\boldsymbol{q}^T = \{q, 0, 0, 0, 0, 0, 0, 0\}$ and differentiating Equation (1b), Equation (1) can be rewritten in the matrix form:

$$\mathbf{E_0}\frac{\partial \mathbf{u}}{\partial t} = \mathbf{A_0}\frac{\partial \mathbf{u}}{\partial x} + \mathbf{B_0}\frac{\partial \mathbf{u}}{\partial y} + \mathbf{C_0}\mathbf{u} + \mathbf{q} \tag{4}$$

where

$$\mathbf{E_0} = \begin{bmatrix} \rho h & 0 & 0 & 0 & 0 & 0 & 0 & 0 \\ 0 & \frac{\rho h^3}{12} & 0 & 0 & 0 & 0 & 0 & 0 \\ 0 & 0 & \frac{\rho h^3}{12} & 0 & 0 & 0 & 0 & 0 \\ 0 & 0 & 0 & \frac{1}{\kappa^2 Gh} & 0 & 0 & 0 & 0 \\ 0 & 0 & 0 & 0 & \frac{1}{\kappa^2 Gh} & 0 & 0 & 0 \\ 0 & 0 & 0 & 0 & 0 & \frac{1}{(1-\nu^2)D} & -\frac{\nu}{(1-\nu^2)D} & 0 \\ 0 & 0 & 0 & 0 & 0 & -\frac{\nu}{(1-\nu^2)D} & \frac{1}{(1-\nu^2)D} & 0 \\ 0 & 0 & 0 & 0 & 0 & 0 & 0 & \frac{2}{(1-\nu)D} \end{bmatrix}$$

$$\mathbf{A_0} = \begin{bmatrix} 0 & 0 & 0 & 0 & 1 & 0 & 0 & 0 \\ 0 & 0 & 0 & 0 & 0 & 1 & 0 & 0 \\ 0 & 0 & 0 & 0 & 0 & 0 & 0 & 1 \\ 0 & 0 & 0 & 0 & 0 & 0 & 0 & 0 \\ 1 & 0 & 0 & 0 & 0 & 0 & 0 & 0 \\ 0 & 1 & 0 & 0 & 0 & 0 & 0 & 0 \\ 0 & 0 & 0 & 0 & 0 & 0 & 0 & 0 \\ 0 & 0 & 1 & 0 & 0 & 0 & 0 & 0 \end{bmatrix}$$

$$\mathbf{B_0} = \begin{bmatrix} 0 & 0 & 0 & 1 & 0 & 0 & 0 & 0 \\ 0 & 0 & 0 & 0 & 0 & 0 & 0 & 1 \\ 0 & 0 & 0 & 0 & 0 & 0 & 1 & 0 \\ 1 & 0 & 0 & 0 & 0 & 0 & 0 & 0 \\ 0 & 0 & 0 & 0 & 0 & 0 & 0 & 0 \\ 0 & 0 & 0 & 0 & 0 & 0 & 0 & 0 \\ 0 & 0 & 1 & 0 & 0 & 0 & 0 & 0 \\ 0 & 1 & 0 & 0 & 0 & 0 & 0 & 0 \end{bmatrix}$$

$$\mathbf{C_0} = \begin{bmatrix} 0 & 0 & 0 & 0 & 0 & 0 & 0 & 0 \\ 0 & 0 & 0 & 0 & -1 & 0 & 0 & 0 \\ 0 & 0 & 0 & -1 & 0 & 0 & 0 & 0 \\ 0 & 0 & 1 & 0 & 0 & 0 & 0 & 0 \\ 0 & 1 & 0 & 0 & 0 & 0 & 0 & 0 \\ 0 & 0 & 0 & 0 & 0 & 0 & 0 & 0 \\ 0 & 0 & 0 & 0 & 0 & 0 & 0 & 0 \\ 0 & 0 & 0 & 0 & 0 & 0 & 0 & 0 \end{bmatrix}$$

Finite difference algorithm

A higher order finite difference algorithm developed by MacCormack is used in this study to simulate the A_0 reflection waves, which is available in Matlab.[24,27,30] When the initial condition at time step n is given by $\mathbf{U^n} = \mathbf{E_0}\mathbf{u^n}$, the output value of the next time step U^{n+2} can be expressed using the MacCormack splitting method as

$$\mathbf{U^{n+2}} = F_x F_y F_y^+ F_x^+ \mathbf{U^n} \tag{5}$$

where F_x and F_y are the backward–forward operators in x- and y-direction, and F_x^+ and F_y^+ are the forward–backward operators in x- and y-direction.

Although the explicit finite-difference scheme is computationally much more efficient than the implicit scheme, it is restricted by CFL (Courant–Friedrichs–Lewy) stability condition. CFL stability condition assumes that the waves are not allowed to propagate over two grids in just a single time step, so that the properties of the waves can be preserved in the numerical approximation and the stability is guaranteed. It requires

the numerical propagation speed $\Delta x/\Delta t$ to be less than fastest wave propagation. For the MacCormack scheme, the time step is limited by

$$\Delta t < \frac{2\Delta x}{3v_{\max}} \tag{6}$$

With $v_{\max} \approx 3000\,\text{m/s}$ and $\Delta x = 1.25\,\text{mm}$, the time step is chosen to be 0.2 μs. Therefore, the total time of simulation is 250 μs with 1250 steps, which corresponds to a 5 MHz sampling frequency in the experiment. Material properties given in Table 1 were used, and the grid covered only the $500 \times 500\,\text{mm}^2$ area as shown in Figure 1(a), since there is no point simulating wave propagation outside the sensor array region. The plate is discretized by a 400×400 rectangular grid, with grid spacing of 1.25 mm, and the excitation points and sensor positions are identical to the center point of the sensors used in the experiment. Figure 6(a) shows a snapshot of the displacement field during simulation, where the excitation source for this case is the origin.

In the damaged plate simulation, the crack is modeled by altering the property matrix $\mathbf{E_0}$ at the corresponding grid points. The crack size is also increased in 15 steps; at each increment, a five-peaked tone burst signal is emitted from the excitation grid and the wave signal is collected from grids at all other sensors positions along the horizontal line (x-axis). Figure 6(b) shows a snapshot of wave field in the damaged plate, where we can observe the scattered wave field. Boundary reflection is present, but is much weaker than the visualized signal at $t = 100\,\mu\text{s}$.

Image construction for location

The scattered signal amplitude depends strongly on the sensor location, because cracks closer to the sensor array produce waves with larger amplitudes than cracks farther. Estimating the location of a crack can be done by creating images with available techniques. We used the f–k migration technique,[26,27] a method to image damage using scattered wave fields obtained at sensors within a planar structure. In the f–k migration technique, image intensity for one grid is calculated using the cross-correlation between the incident wavefield and scattered wavefield at a given time, and the final image is obtained by assessing the image intensity value at every grid. An example of scattered wavefield is shown in Figure 7(a), and the corresponding incident wavefield is shown in Figure 7(b). By Equation (7), we can find the cross-correlation coefficient at each sensor position and at each time difference, and the information is integrated into one image.

$$\Phi_{fg}(t) = (f^* g)(t) = \int_{-\infty}^{\infty} f^*(\tau) \cdot g(t+\tau)\mathrm{d}\tau$$
$$\Phi_{fg}(t)_{norm} = \frac{\Phi_{fg}(t)}{\sqrt{\Phi_{ff}(0) \cdot \Phi_{gg}(0)}} \tag{7}$$

where f is the scattered wavefield at each sensor position, f^* is its complex conjugate, g the incident wavefield emitted from the actuator, and t the time difference.

For example, if time difference between scattered signal and incident wavefield at sensor position

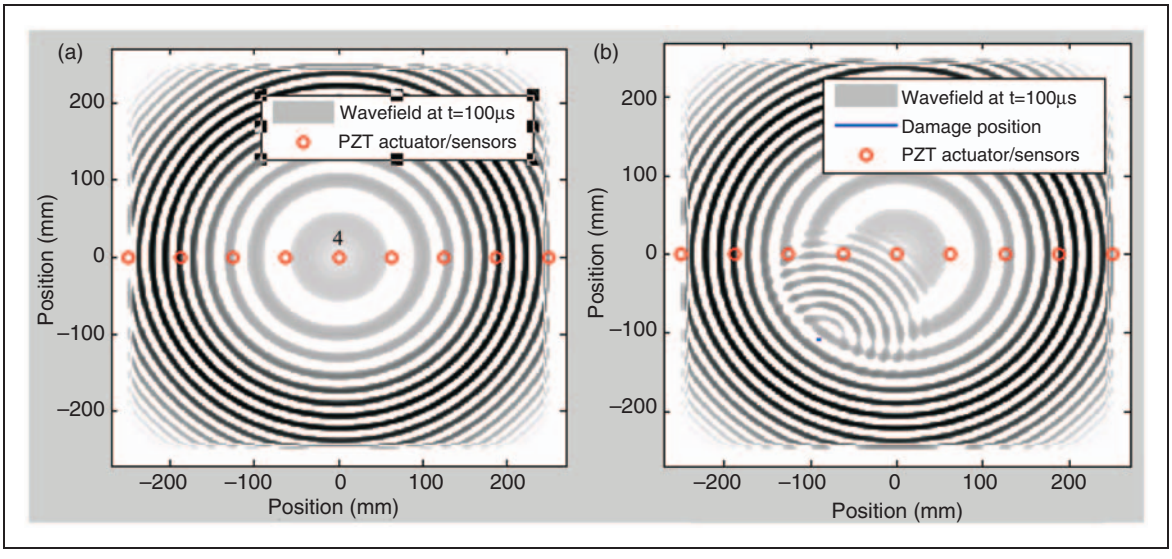

Figure 6. (a) Snapshot of the simulated structural wave propagating in the pristine plate at $t = 100\,\mu\text{s}$. The toneburst wave is emitted from actuator 4. (b) Snapshot of the wave in the damaged plate at $t = 100\,\mu\text{s}$. The crack is 0.25 mm and located at (−90, −110) mm from the origin.

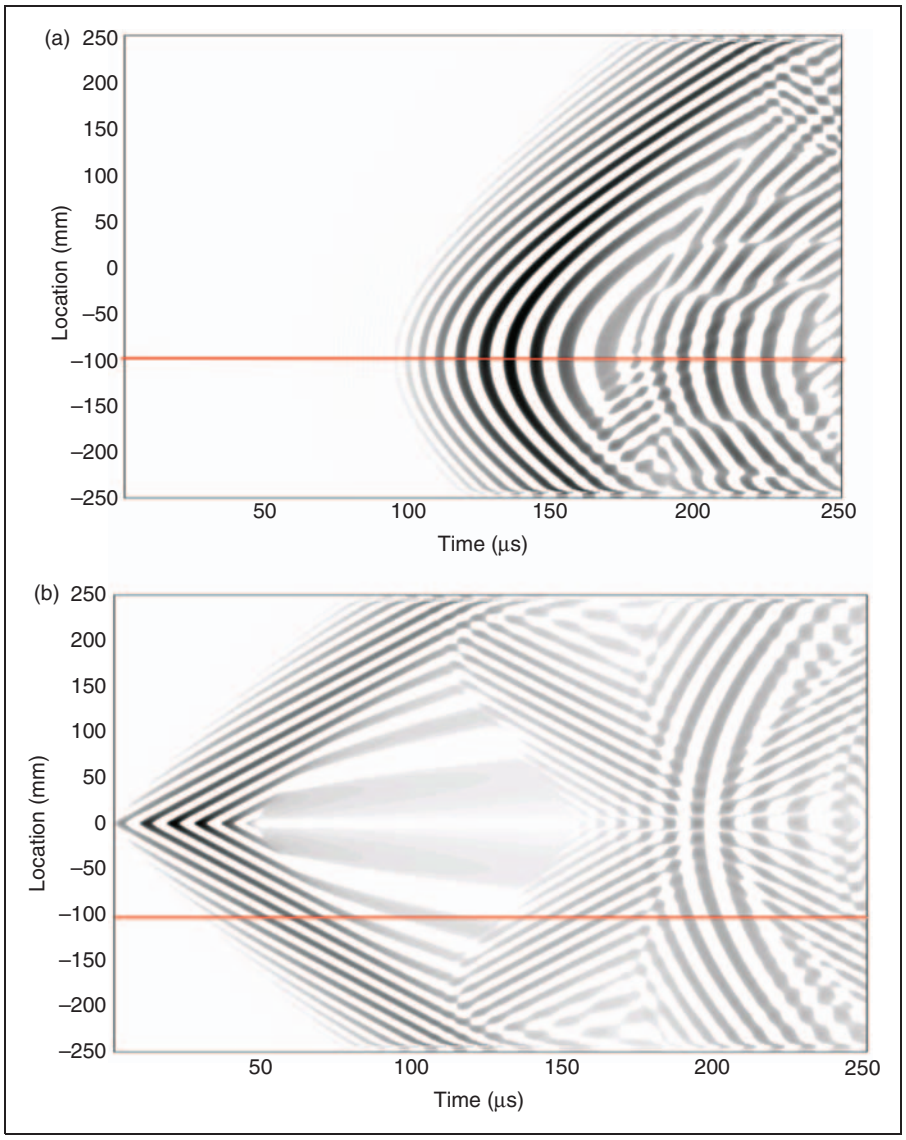

Figure 7. (a) Scattered wavefield and (b) incident wavefield.

−100 mm is 40 μs, then the cross-correlation coefficient is measured by Equation (7), and the image intensity value at the position (−100, −120) mm is assigned with the coefficient.

One image is created from each toneburst excitation. In the experiment and simulation, we used seven excitation sources to emit or simulate the wavefield, and we created seven images, which were combined into the final image using the prestack approach from the migration technique.[23] In simulation and experiment, there are nine PZTs of which one is an actuator and the other eight are sensors. We used spline interpolation to generate the scattered wave field at points between sensors. In Figure 8, we demonstrated the identification of approximate location of the crack with the given sensor signal, and showed the approximate crack center location by the maximum intensity location in Table 4. The estimated locations were compared with the true location in Table 4.

Results

Scattered signal from the damage

In simulation, the transverse velocity is chosen as the sensing parameter at the corresponding nodes, and the maximum amplitude is proportional to the maximum strain or voltage at each piezoelectric transducer disc in the experiment. In both simulation and experiment, the scattered signal is obtained by subtracting the pristine plate signal from the damaged plate signal. Figure 9 displays a sample case when the crack size is 26 mm

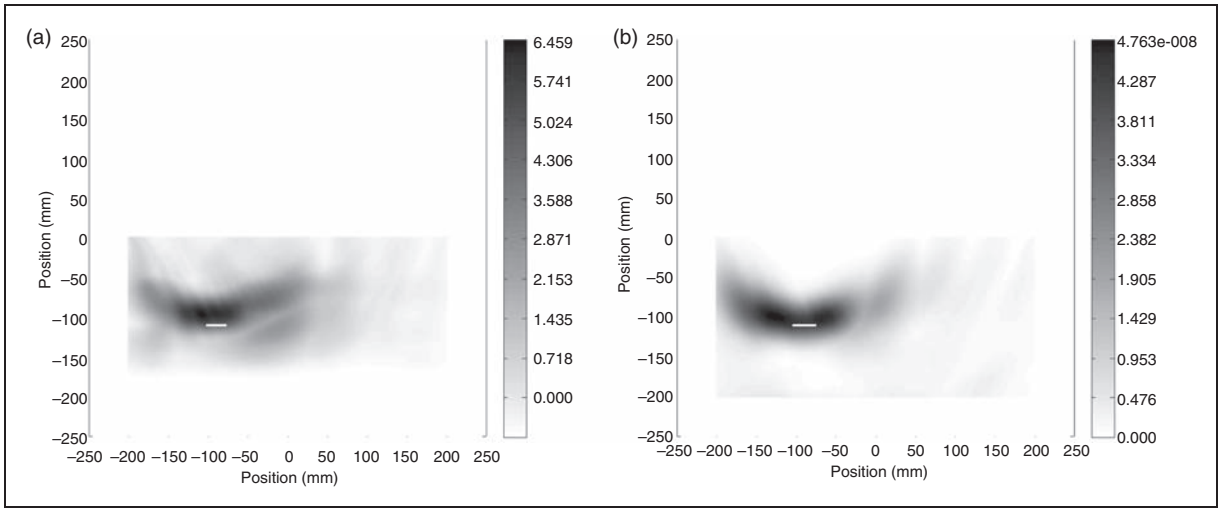

Figure 8. Image produced by migration technique. The crack size is 26 mm (a) experimental results are reproduced into image and (b) simulation result using eight sensors.

Table 4. Crack locations estimated from the image by the maximum intensity

	Crack center location (mm)	Distance from true crack center (mm)
True	−90, −110	
Experiment (Figure 8(a))	−97.5, −105.0	9.0
Simulation (Figure 8(b))	−87.5, −107.5	3.5

and the excitation point is at actuator 4, which is located at the center of the plate (Figure 1).

In Figure 9, symmetry between left and right sides of actuator 4 was expected and observed in the simulation, but the experiment showed substantial asymmetry. This is attributed to differences in individual sensor quality and attachment uniformity. However, we have observed reasonable agreement between simulation and experiment in terms of TOF and scattered signal amplitude.

Change in the signal with crack size

Maximum peak-to-peak amplitude of a signal represents the maximum strain energy transfer rate by the given signal. By examining the maximum peak-to-peak amplitude of the scattered signal, we can observe that the amplitude increases with crack size. Figure 10 shows the change in the scattered signal amplitude for two different crack sizes.

We have seven excitation sources, and for each excitation, eight sensors are used to examine the scattered signal. The highest peak-to-peak amplitude among all sensors and actuators is the maximum signal amplitude for each crack size. The maximum amplitude occurred usually at actuator 3 and sensor 2 for all crack sizes, except that for cracks sizes 2.5, 3, and 4.5 mm it happened at actuator 4 and sensor 2. Due to difficulty in modeling the actuator and sensor interaction with the plate, normalized measured signals are compared to normalized signal velocities. Without loss of generality, the data are normalized with respect to the signal amplitude when the crack size is 25 mm. The comparison between normalized values of signal amplitude is presented in Figure 11. It can be seen that the relation is proportional to the crack size of 30 mm, and showed a good agreement between experiment and simulation.

The major observation in this experiment is that the signal amplitude increases with crack size up to a saturation point. This provides us a capability to monitor a crack growth up to a certain size.

Effect of frequency

Figure 11 shows divergence of signal amplitudes between measurement and simulation when the crack size is longer than 30 mm. To investigate this further, the experiment was repeated using a different excitation frequency. Since the signal from the experiment has both S_0 and A_0 mode, we examined individual signal to determine which is dominant. This is possible because S_0 mode is significantly faster than A_0 mode (Figures 10 and 12).

While the signal amplitude of S_0 and A_0 mode has similar magnitude for this central frequency, we observed that A_0 mode amplitude is still larger than S_0 mode in the scattered signal (Figure 12).

The result, obtained at the same crack sizes with a different central frequency of 150 kHz, is presented in

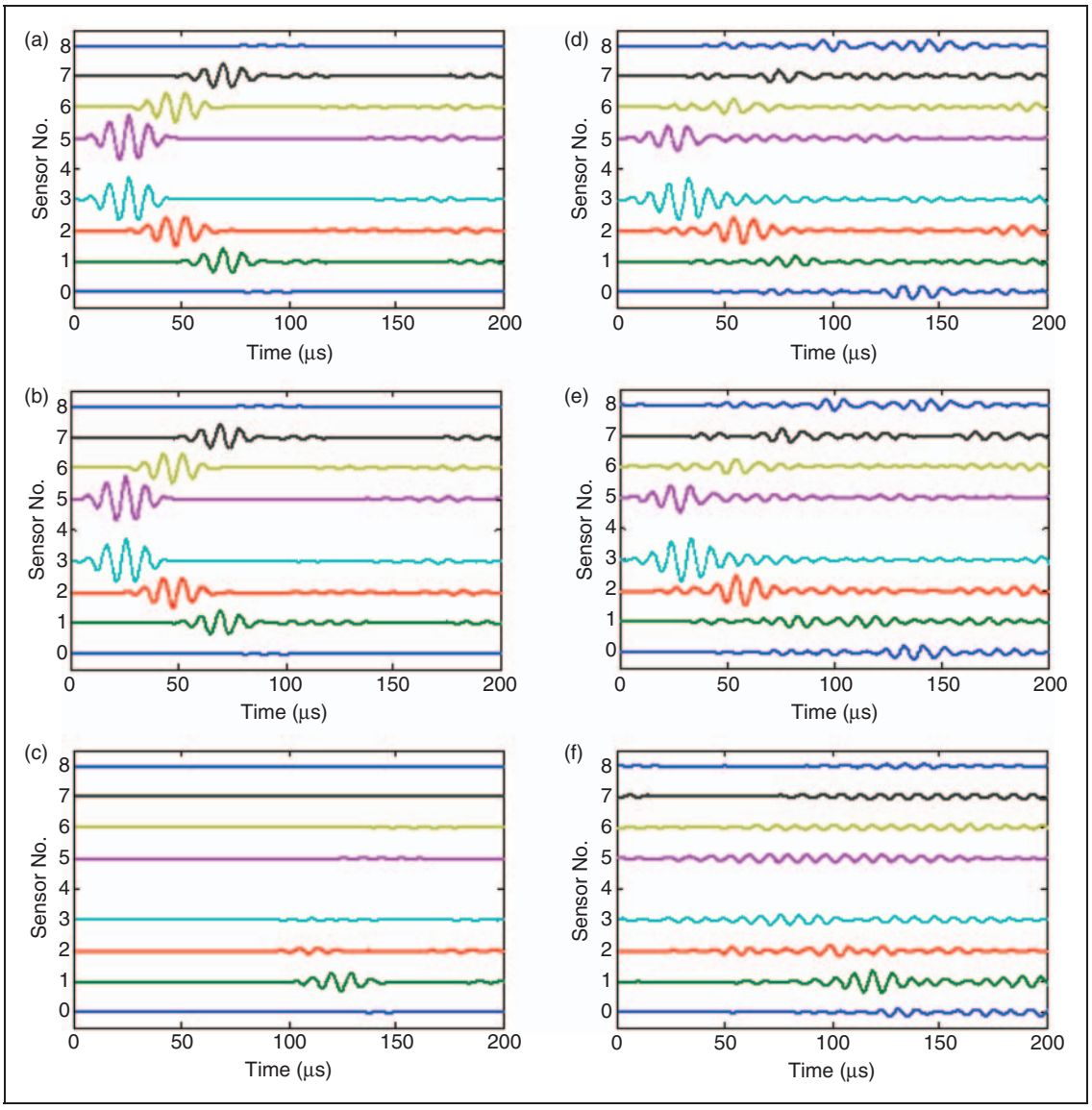

Figure 9. Toneburst excitation is emitted from actuator 4, and measured from all eight sensors from simulation (a–c) and experiment (d–f). Sensor spacing is 62.5 mm each. (a) Pristine plate signal; (b) damaged plate signal; (c) scattered signal by subtracting (a) from (b). We can observe the scattered signal from the boundaries in experiment, but it is almost completely removed after subtraction. (d) Pristine plate; (e) damaged plate; and (f) scattered signal by subtracting (a) from (b). (Signal amplitude is adjusted for (c) and (f) because the scattered signal is much smaller than the healthy or damaged ones).

Figure 13. The amplitudes are normalized by the same scale factor as the previous result. In this case, the agreement between experiment and simulation was maintained up to crack size of 22 mm.

This time the separation between the two graphs occurs around 22 mm. We speculate that is related to the wavelength (150 kHz, A_0 mode wavelength $\lambda \approx 20$ mm, and 110 kHz, $\lambda \approx 27$ mm). Since all other conditions are identical and the group velocity of A_0 mode propagation in the plate is almost the same for both frequencies, we concluded that the agreement may deteriorate for crack sizes larger than the wavelength. Also, the signal amplitude behavior beyond this point may be due to geometrical discrepancies; for example, the crack tested in the experiment is not perfectly straight. For longer cracks, the geometric variations are responsible for the change in the maximum amplitude by changing the amplitude along the directions of scattered waves. In other words, we require more precise modeling for better agreement between simulation and experiment. The main reason that we do not discuss further on this effect is that we still can cover a wider range by changing the excitation frequency. However, when we are interested in long cracks, we can estimate

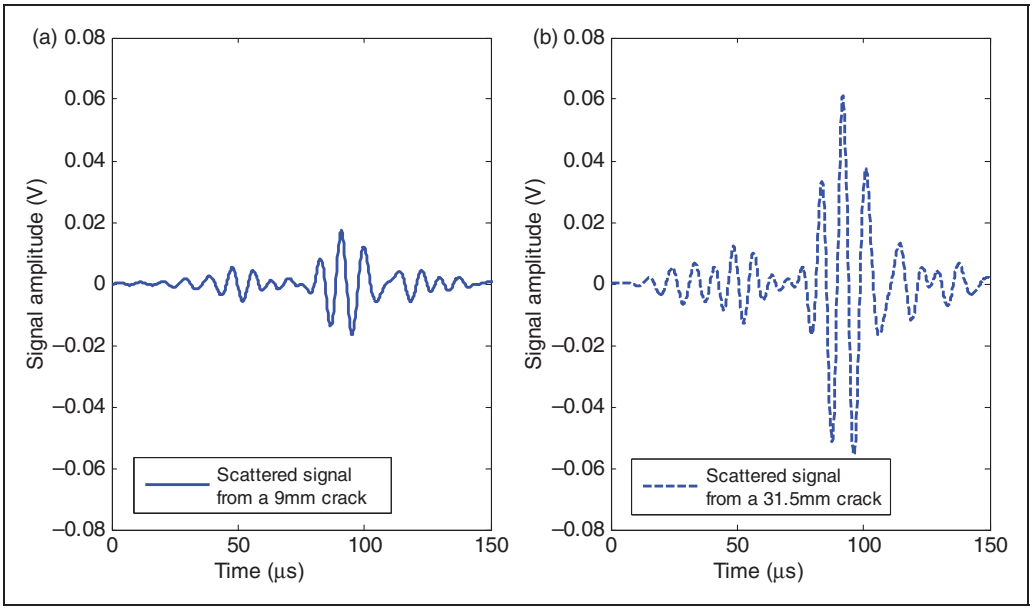

Figure 10. Experimental scattered signal amplitude change in different size cracks. (a) 9 mm and (b) 31.5 mm.

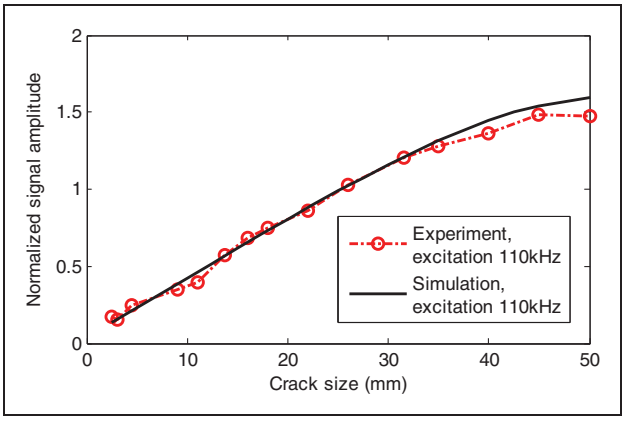

Figure 11. Signal amplitude variation (maximum peak-to-peak amplitude). The excitation frequency is 110 kHz and the signal amplitude is normalized using the signal at crack size 25 mm as the reference.

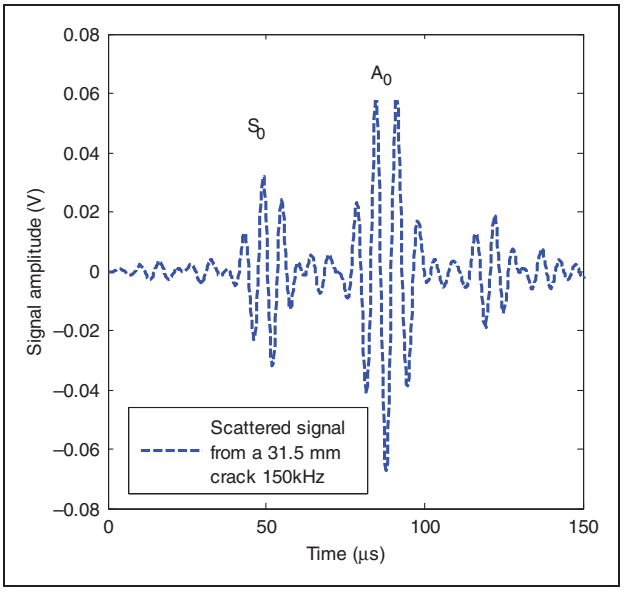

Figure 12. Scattered signal amplitude with 150 kHz excitation.

the size by processing images obtained from migration technique or other techniques for general crack shapes; 11 mm crack also showed an abnormal result, but it is probably due to the transition from a circular hole to a hole plus a machined crack around that size.

Crack location effect

We next investigated the effect of the relative location of the crack and the sensor array. Figure 14(a) shows two sensor arrays on a single plate and the simulation domain covered by each array. The crack is located at (−90 mm, −110 mm) from sensor 4 of array 1, while it is located at (−100 mm, −140 mm) from sensor 4 of array 2. The experiment for two different domains is essentially equivalent to cases for two different crack locations (Figure 14(b)). The behavior of maximum signal amplitude is predicted by simulation, and obtained from experiment. By using sensor array 2, we were able to obtain the signal amplitude for crack position 2, and compared it with the simulation results in Figure 15.

Since the distance from the sensor array is larger, the slope of peak-to-peak amplitude to the crack size is

smaller compared to the previous experiment, but slightly larger than expected from the simulation. The sensors have some variability, so the sensors used later might be more sensitive than the one used in Figure 11. Therefore, a different crack location as well as the sensors require a different calibration factor, which represents a different slope between crack size and signal amplitude. In our case, the factor is not calculated but we have performed another simulation to find more accurate relation. With the updated predicted behavior, we were able to find a linear relationship between signal amplitude and the crack size for the second location.

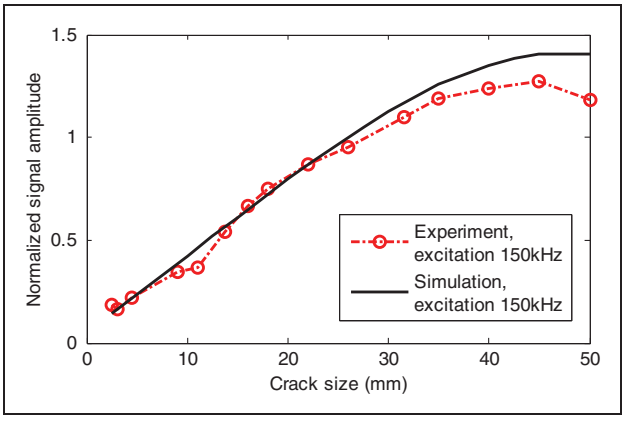

Figure 13. Signal amplitude variation (maximum peak-to-peak amplitude). The excitation frequency is 150 kHz and the signal amplitude is normalized using the same scale factor as Figure 11.

Since approximate crack location may be found by the migration technique, the calibration factor, or the coefficient for the linear relation, can also be found from that information. However, uncertainty in sensor characteristics and estimated location may be encountered during the procedure. To implement an SHM system to real-life structures, more research has to be done to overcome these difficulties.

Concluding remarks

In this article, we have shown how we can find crack location through images based on the migration technique, and we explored the effect of increasing crack size on scattered signal amplitude in a plate structure at that location by simulation and experiment.

By testing a series of crack sizes using ultrasonic Lamb waves, we have found that the scattered signal amplitude is linearly proportional to crack size in the case of a straight crack up to a certain size. This means that the scattered signal amplitude provides an inference for crack size estimation. For large cracks, the proportionality breaks down. By checking for two different central frequencies, we observed that the proportionality appears to break down when the crack size is close to the wavelength.

This article utilizes signal amplitude to measure crack sizes. We have shown that the increasing signal amplitude can indicate crack propagation. This approach may provide a useful inference about a small crack, whose size is difficult to measure with other techniques.

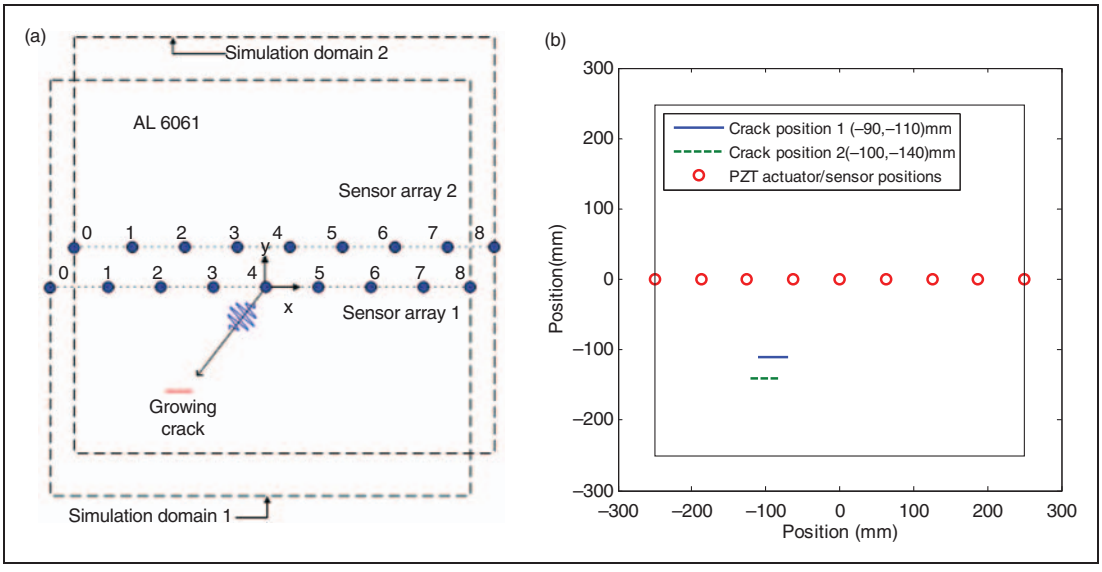

Figure 14. (a) Two sets of sensors and the domains covered by each array and (b) different crack center location with respect to the actuator positions: second crack center location is (−100 mm, −140 mm).

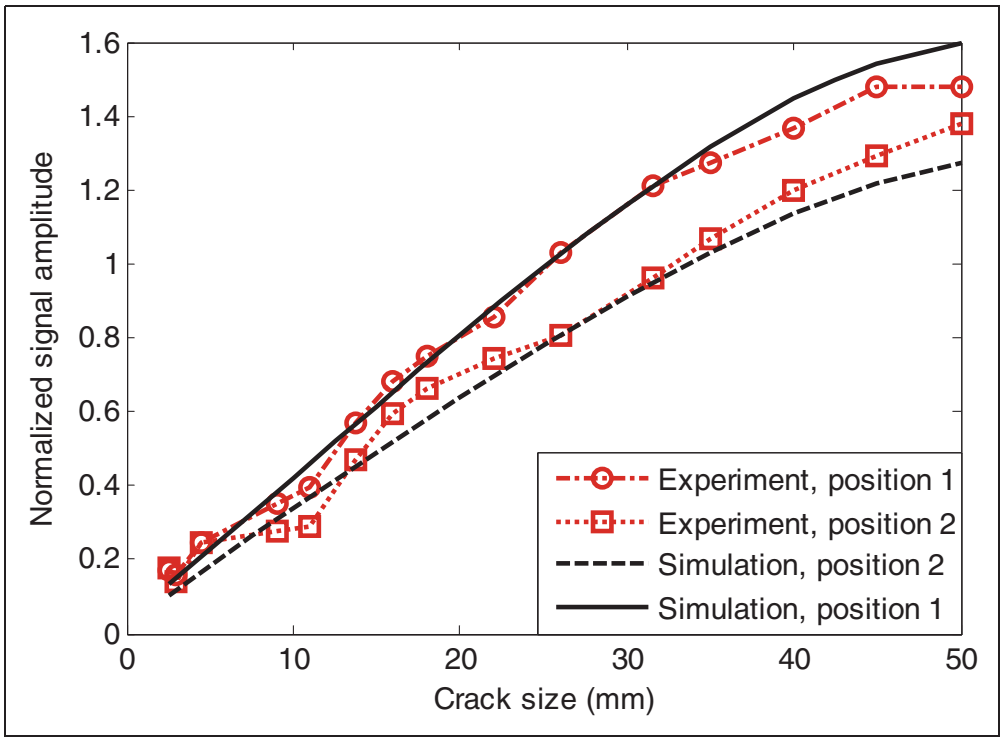

Figure 15. Scattered signal amplitude variation for cracks growing at a different location excited by 110 kHz ultrasonic toneburst. Signal amplitude comparison with result shown in Figure 11, simulation and experiment. The crack positions are shown in Figure 14.

Acknowledgments

The authors gratefully acknowledge the support for the research provided by the NASA [grant number: NNX08AC334]; and the United States Air Force, Air Force Research Laboratory [grant number: FA9550-07-1-0018].

References

1. Papazian JM, Anagnostoua EL, Engela SJ, et al. A structural integrity prognosis system. *Eng Fract Mech* 2009; 76(5): 620–632.
2. Sohn H, Farrar CR, Hemez FM, et al. (2004). A review of structural health monitoring literature: 1996–2001. Report Number LA-13976-MS, Los Alamos National Laboratory, Los Alamos, NM.
3. Giurgiutiu V. *Structural health monitoring with piezoelectric wafer active sensors*. San Diego and London: Academic Press, 2008.
4. Raghaven A and Cesnik CES. Review of guided-wave structural health monitoring. *Shock Vib Digest* 2007; 39(2): 91–114.
5. Giurgiutiu V and Cuc A. Embedded NDE for structural health monitoring, damage detection, and failure prevention. *Shock Vib Rev* 2005; 37(2): 83–105.
6. Doebling SW, Farrar CR and Prime MB. A summery review of vibration-based damage identification methods. *Shock Vib Dig* 1998; 30(2): 91–105.
7. Montalvão D, Maia NMM and Ribeiro AMR. A review of vibration-based structural health monitoring with special emphasis on composite materials. *Shock Vib Digest* 2006; 38: 295.
8. Zou Y, Tong L and Steven GP. Vibration-based model-dependent damage (delamination) identification and health monitoring for composite structures - a review. *J Sound Vib* 2000; 230(2): 357–378.
9. Sodano HA. Development of an automated eddy current structural health monitoring technique with an extended sensing region for corrosion detection. *Struct Health Monit* 2007; 6(2): 111–119.
10. Banks HT, Joyner ML, Wincheski B and Winfree WP. Real time computational algorithms for eddy-current based damage detection. *Inverse Prob* 2002; 18(3): 795–823.
11. Zhou G and Sim LM. Damage detection and assessment in fibre-reinforced composite structures with embedded fibre optic sensors—review. *Smart Mater Struct* 2002; 11: 925–939.
12. Charlesworth JP and Temple JAG. *Engineering applications of ultrasonic time of flight diffraction*. London: Research Studies Press Ltd, 1989.
13. Fromme P. (2002). Defect detection in plates using guided waves.Swiss Federal Institute of Technology, Doctoral Thesis.
14. Ritdumrongkul S and Fujino Y. Identification of the location and size of cracks in beams by a piezoceramic actuator–sensor. *Struct Control Health Monit* 2007; 14: 931–943.

15. Lu Y, Ye L and Su Z. Crack identification in aluminum plates using Lamb wave signals of a PZT sensor network. *Smart Mater Struct* 2006; 15: 839–849.
16. Michaels JE and Michaels TE. Detection of structural damage from the local temporal coherence of diffuse ultrasonic signals. *IEEE Trans Ultrason Ferroelectr Freq Control* 2005; 52(10): 1769–1782.
17. Ihn JB and Chang FK. Pitch-catch active sensing methods in structural health monitoring for aircraft structures. *Struct Health Monit* 2008; 7(5): 5–19.
18. Douka E, Loutridis S and Trochidis A. Crack identification in plates using wavelet analysis. *J Sound Vib* 2004; 270: 279–295.
19. Kerbrat E, Clorennec D, Prada C, Royer D, Cassereau D and Fink M. Detection of cracks in a thin air-filled hollow cylinder by application of the DORT method to elastic components of the echo. *Ultrasonics* 2002; 40: 715–720.
20. Malinowski P, Wandowski T, Trendafilova I and Ostachowicz W. A phased array-based method for damage detection and localization in thin plates. *Struct Health Monit* 2009; 8: 5–15.
21. Yan F, Royer Jr RL and Rose JL. Ultrasonic guided wave imaging techniques in structural health monitoring. *J Intell Mater Syst Struct* 2010; 21: 377–384.
22. Giurgiutiu V. Tuned lamb wave excitation and detection with piezoelectric wafer active sensors for structural health monitoring. *J Intell Mater Syst Struct* 2005; 16: 291–305.
23. Sicard R, Chahbaz A and Goyette J. Guided lamb waves and l-saft processing technique for enhanced detection and imaging of corrosion defects in plates with small depth-to-wavelength ratio. *IEEE Trans Ultrason Ferroelectr Freq Control* 2004; 51(10): 1287–1297.
24. Wang L and Yuan FG. Damage identification in a composite plate using prestack reverse-time migration technique. *Struct Health Monit* 2005; 4(3): 195–211.
25. Lin X and Yuan FG. Experimental study applying a migration technique in structural health monitoring. *Struct Health Monit* 2005; 4(4): 341–353.
26. Zhou L, Yuan FG and Meng WJ. A pre-stack migration method for damage identification in composite structures. *Smart Struct Syst* 2007; 3(4): 439–454.
27. Lin X and Yuan FG. Damage detection of a plate using migration technique. *J Intell Mater Syst Struct* 2001; 12: 469–482.
28. An J, Haftka RT, Kim N, Yuan FG and Kwak BM. Bayesian approach for structural health monitoring – application to migration technique. *US-Korea Workshop on Bio-Inspired Sensor Technology and Infrastructure Monitoring*. Korea.
29. An J, Haftka RT, Kim N, Yuan FG and Kwak BM. Compensation for decay of signal strength in damage detection by ultrasonic imaging: application to migration technique. In: *50th AIAA/ASME/ASCE/AHS/ASC Structures, Structural Dynamics, and Materials Conference,* Palm Springs, California, 2009.
30. Bayliss A, Jordan KE, LeMesurier BJ and Turkel E. A fourth-order accurate finite-difference scheme for the computation of elastic waves. *Bull Seismol Soc Am* 1986; 76(4): 1115–1132.